PAPER • **OPEN ACCESS**

Reduced trap-density and boosted performance of $CH_3NH_3PbI_3$ solar cells by 1-Pentanethiol enhanced anti-solvent washing route

To cite this article: F Pinar Gokdemir Choi *et al* 2024 *Nanotechnology* **35** 215401

View the article online for updates and enhancements.

You may also like

- Wash-out of ambient air contaminations for breath measurements
F Maurer, A Wolf, T Fink et al.
- A review of exhaled breath: a key role in lung cancer diagnosis
Davide Marzorati, Luca Mainardi, Giulia Sedda et al.
- Measurement of pentane in expiratory gas during rabbit hepatic ischemia/reperfusion by solid-phase microextraction and gas chromatography–mass spectrometry (SPME GC/MS)
Shujuan Liu, Jinghui Shi, Changsong Wang et al.



This content was downloaded from IP address 193.140.1.200 on 18/03/2024 at 20:01

OPEN ACCESS
IOP Publishing
Nanotechnology
Nanotechnology **35** (2024) 215401 (10pp)
https://doi.org/10.1088/1361-6528/ad2a00

Reduced trap-density and boosted performance of $CH_3NH_3PbI_3$ solar cells by 1-Pentanethiol enhanced anti-solvent washing route

F Pinar Gokdemir Choi[1,*], Furkan Kuruoğlu[2,*], Hamed Moeini Alishah[1], Sinem Bozar[3], Cihangir Kahveci[1], Macide Canturk Rodop[1], Ayse Erol[2] and Serap Gunes[1]

[1] Yildiz Technical University, Faculty of Arts and Science, Department of Physics, Davutpasa Campus, 34210, Esenler, Istanbul, Turkey
[2] Istanbul University, Faculty of Science, Department of Physics, Vezneciler, Istanbul, Turkey
[3] Istanbul Technical University, Energy Institute, Istanbul, Turkey

E-mail: pinargokdemir1984@gmail.com and furkan.kuruoglu@istanbul.edu.tr

Received 5 October 2023, revised 30 December 2023
Accepted for publication 16 February 2024
Published 6 March 2024

Abstract

Performance and the stability of the perovskite-based photovoltaic devices are directly linked to existing trap-states or defect profiles at the surface and/or in the bulk of perovskite layers. Hence identification of stemming the defects during perovskite formation is crucial for achieving superior and long-lasting performances. Here, we present the effect of 1-Pentanethiol incorporation into the one-step deposition of perovskite layers. A feasible glove box-free route results in high-quality $CH_3NH_3PbI_3$ layers under highly humid conditions ($RH > 50\%$) but at low temperatures ($T < 18\ ^{\circ}C$). 1-Pentanethiol addition into the washing solvent leads to the refinement of I/Pb stoichiometry, elimination of the iodide deficiencies, and reduction of the trap-state densities. Consequently, a precise amount 1-Pentanethiol addition enhances photovoltaic performances, resulting in a 54% PCE improvement for $CH_3NH_3PbI_3$-based inverted solar cells.

Supplementary material for this article is available online

Keywords: 1-Pentanethiol, uncoordinated Pb^{2+}, defect passivation, $CH_3NH_3PbI_3$, inverted solar cells, glove box free, perovskite

Introduction

Generating energy via cost and energy-effective ways has become one of the biggest challenges of today. Production of electrical energy using solar cells has been one of the most popular of these costs and energy-efficient ways. Recently, perovskite solar cells fabricated using hybrid metal halide perovskite materials have become the rising star of today's solar cell technologies. The increase in their power conversion efficiencies from the modest values to a certified value of 25.2% by Seo *et al* [1] in a very short time has made them a promising solar cell technology. Two types of perovskite solar cells named normal (n–i–p) and inverted (p−i–n) in planar structure have been realized up to now. First planar heterojunction solar cells have been realized by Jeng *et al* [2], using PEDOT:PSS substrate as a positive electrode and $CH_3NH_3PbI_3$ perovskite/fullerene (C_{60}) structure as the

* Authors to whom any correspondence should be addressed.

Original content from this work may be used under the terms of the Creative Commons Attribution 4.0 licence. Any further distribution of this work must maintain attribution to the author(s) and the title of the work, journal citation and DOI.

© 2024 The Author(s). Published by IOP Publishing Ltd

active layer with moderate efficiencies of 3.9%. They drew attention to the thickness and morphology of the perovskite layer and mentioned that the morphology of the perovskite layer by choosing the appropriate solvent, concentration, preheating temperature, etc would be expected to further increase the device performance. Since then several studies performed on perovskite solar cells addressed that for further improvement of the PCEs of perovskite solar cells, the morphology of the perovskite layer plays an important role [3]. Except for the thermal evaporation and hybrid routes [4, 5], there are mainly solvent-engineering methods that can be divided into two such as one-step and two-step coating [6, 7]. Both of them have advantages where two-step routes provide more controlled crystallization [7] and one-step routes come with simplicity, low-temperature processing [8], and greater reproducibility [9]. It is comprehended that the dominated film formation procedure is crystal growth and nucleation for one-step and two-step routes, respectively [9].

In one-step routes, perovskite precursors are directly spin-coated onto the related substrate and mostly an anti-solvent drowned out during spinning [10, 11]. The main reason behind this step is to remove the perovskite precursor's host solvent/solvents and start the crystallization process, in other words, to reduce or slow down the solubility of perovskite in the precursor to induce higher levels of supersaturation thus nucleation, which is followed by new crystalline formations [12, 13]. Hence for the anti-solvent washing-based routes, type of the washing solvent, compatibility with the perovskite precursor, washing time, volume [14], washing speed [15], temperature of both substrate and washing solvent [16] in addition to the ambient atmosphere, play crucial roles to obtain high-quality perovskite layer growth [13, 17–20]. Various types of anti-solvents, their mixtures, and also with additives have been employed and resulted in superior PCEs even though they have diverse physicochemical properties. Recently, Taylor *et al*, investigated anti-solvent washing over 14 different solvents and stated that optimal application time and rate that can eliminate excess PbI_2 in the perovskite precursor might result in favorable PCEs with any type of solvent [13]. They divided anti-solvents into the first type (ethanol, isopropanol, butyl alcohol), second type (ethyl acetate, chloroform, chlorobenzene, butyl acetate, dichlorobenzene, anisole, trifluorotoluene), and third type (diethyl ether, m-xylene, toluene, mesitylene) series. This categorization is based on washing solvents' strength to dissolve the related organic ingredients and their miscibility with the perovskite precursor's host solvent. The first type series was found to be successful in the case of fast washing procedures while the third type series provided the best perovskite formation qualities under slow washing. Apart from the process of the anti-solvent washing, employing novel additives within perovskite precursor solution or in washing anti-solvent have been investigated and found to affect crystallization, film formation, band structure, and also defect characteristics of the perovskite [21]. Popular additives can be classified as ionic liquids, Lewis acids, and bases [22]. Owing to their electrostatic strength and compatibility with perovskite precursors components, ionic liquids enhance the growth quality of perovskite layers [23]. When it comes to Lewis acids (metal cations and fullerenes), they are known to passivate electron-rich type defects which are originating from excess halides [24]. Besides, Lewis bases help to form Lewis adducts by correlating with uncoordinated Pb^{2+} [25–27]. Sulfur-related materials including sulfur atoms are labeled as Lewis bases and sulfur works as a better electron-donating agent compared to oxygen and nitrogen [28, 29]. Hence sulfur-based materials are engaged as a compositional regulation agent, precursor stabilizer [30], additive, and/or as an interface modifier to enhance the phase stability [31] and/or passivate the perovskite [32, 33].

Thiols or thiol derivatives are a member of an organo-sulfur family with the form R-SH where R is an alkyl and −SH is the organic functional (sulfhydryl or sulfanyl) group. Cao *et al*, studied the modification of $CH_3NH_3PbI_3$ and TiO_2 electron transport layer (ETL) interface employing thiols (pentafluorobenzenethiol) and reported improved stability and performance of the perovskite solar cells (PSCs) [34]. This enhancement is associated with the increase in electron transfer from perovskite to ETL which is related to the HOOC-Ph-SH incorporation at the interface and also altered perovskite growth. Chang *et al*, reported that they improved the performance and stability of perovskite solar cells by employing a new cathode buffer layer based on thiol-functionalized cationic surfactant (11-mercaptoundecyl) trimethylammonium bromide. Thiol function groups were told to form Ag–S covalent bonds inducing multi positive outcomes on the interface such as lowered contact resistance also improved thermal stability [35]. Chang *et al*, reported ITO-free PSCs with thiol-functionalized self-assembled monolayers (SAM) to improve the interfacial characteristics [36]. Li *et al*, employed cross-linkable HTL for $CH_3NH_3PbI_3$ based PSCs and included an aliphatic cross-linker (with four thiol groups, PETMP) to overcome the high crosslinking temperature. Their report stated that this promising thermal cross-linking occurs by facile thiol-ene reaction [37]. Xu *et al*, used a CME passivation molecule that has thiol and ester groups, between perovskite and HTL. Results indicated that thiol exhibited notable moisture resistance and ester coordinates with uncoordinated Pb^{2+} [38]. Wu *et al*, employed a thiol-functionalized 2D conjugated metal–organic framework as an ETL at the $Cs_{0.05}(FA_{0.85}MA_{0.15})_{0.95}Pb(I_{0.85}Br_{0.15})_3$/cathode interface [39]. Ruan *et al*, employed alkyl-thiol to form cesium lead halide ($CsPb_2Br_5$) with controlled morphology and a crystalline phase at room temperature [40]. Shi *et al*, inserted a 3-mercaptopropyltrimethoxysilane SAM layer between perovskite and SnO_2 ETL. This interface layer was reported to smoother ETL surface and also slower crystal growth hence resulting in a higher quality of perovskite, passivating the ETL/perovskite interface and enhancing the electron extraction [41]. Xiao *et al* and Li *et al*, studied a post-treatment process for the perovskite layer using thiol copper (II) porphyrin (CuP). Examinations indicated that CuP can anchor the perovskite surface by coordinating with Pb ions through the thiol-terminal of CuP and lower the defect density [42, 43]. To the best of our knowledge, there is no study

related to thiol additive-enhanced washing processes for perovskite layer growth.

Here, we report the profoundly reproducible and efficient PSCs via employing 1-Pentanethiol as an additive into toluene during anti-solvent washing for the one-step deposition of $CH_3NH_3PbI_3$ layers. 1-Pentanethiol is not toxic material and is even used as a food additive. It belongs to the alkyl thiols class containing the thiol functional group linked to an alkyl chain and is an extremely weak basic compound. Another important point is that we have developed a new route that results in high-quality perovskite growth in ambient air under relatively high humidity and low temperature (figure S4(a)). In this one-step route, perovskite precursor is based on the sole gamma-butyrolactone (GBL) host solvent with a stoichiometric PbI_2: MAI (methylammonium iodide) ratio. First, Fateev *et al*, mentioned the lack of understanding of $CH_3NH_3PbI_3$ crystal formation in the case of GBL employed as a host solvent [44]. Without anti-solvent washing, they obtained low-quality perovskite layers including three different types of crystals as needle-like, badly-shaped, and well-shaped tetrahedral. Needle-like structures are explained to display a ribbon-like pattern of face-sharing PbI octahedra and assigned to $(MA)_2(GBL)_2Pb_3I_8$ with a structure similar to the known PbI_2-excessive adducts while badly-shaped ones assigned to the body-centered tetragonal unit cells that consisted of large clusters as $[Pb_{18}I_{44}]^{8-}$. On the other hand, well-shaped tetrahedral crystals were found to be perfectly cubic and combined from two different clusters where half of them were $[Pb_{18}I_{44}]^{8-}$, and the other half were larger disordered clusters with partial occupancy of Pb and I atoms. They concluded that undesired structures can be eliminated for GBL-based routes in the case of precursor solutions have led predominantly in the form of small coordination complexes such as PbI^{3-}. Moreover, they also mentioned that these circumstances can be realized by crystallization of perovskite from hot or MAI excessive GBL solutions, respectively. Their standard anti-solvent (toluene) washing route with a stoichiometric $CH_3NH_3PbI_3$ precursor (kept at room temperature) resulted in pin-hole-dominated perovskite formation. However, by keeping the perovskite precursor solution at 70 °C or employing precursor solution with excessive MAI (PbI_2:MAI 1.0:1.5 M at room temperature) the quality of film formation is enhanced resulting in a perfect coverage and high crystallinity [44]. Later, Huang *et al*, investigated the effect of perovskite precursor host solvents for $CH_3NH_3PbI_3$ formation, using dimethylformamide, gamma-butyrolactone, dimethyl sulfoxide, and the various volumetric mixture of them. PCEs failed for the only DMF-employed devices and were found to be around 1.74% for the only GBL-employed devices which was attributed to the poor coverage of perovskite and low solubility of lead iodide and methylammonium iodide, respectively [19]. Seo *et al*, also investigated the effect of perovskite host solvent type employing GBL, DMF, DMSO, NMP, and mixtures of them. Their report resulted in the lowest PCE around 3.6% for only gamma-butyrolactone employed perovskite precursors with toluene anti-solvent washing mainly associated with the low coverage and inhomogeneity of the perovskite layer [45].

Consequently, as compared to the literature our perovskite layer formation and solar cell performances were accomplished at record values. Moreover, highly promising PCEs values were doubled when 1-Pentanethiol was employed as an additive in toluene anti-solvent washing. Various volumetric ratios of 1-Pentanethiol: toluene were used for perovskite solar cell fabrication and an optimum ratio was found for 0.33% 1-Pentanethiol in toluene. The reason behind this superior enhancement was investigated by x-ray diffraction, scanning electron microscopy, atomic force microscopy, space charge limited current analysis, photoconductivity, photoluminescence, and photovoltaic characterization techniques.

Methods

Starter chemicals for $CH_3NH_3PbI_3$; MAI and PbI_2 were synthesized by our group and details can be found in supporting info.

Materials for PSC fabrication were used without any purification including, 1-Pentanethiol (Sigma 98.0, P7908), gamma-butyrolactone (Across organics γ-Butyrolactone 99+%), toluene (Merck Toluene EMPLURA 108323), chlorobenzene (Merck 801791.2500 Chlorobenzene for synthesis), (Sigma-Aldrich 1,2-Dichlorobenzene anhydrous, 99%), HCl (Merck for analysis EMSURE ACS, ISO, Reag. Ph Eur, Hydrochloric acid fuming 37%), nickel (II) acetate tetrahydrate (Aldrich $>$ 99.0%), MEA (Sigma-Aldrich ethanolamine purified by redistillation, 99.5%), titanium (IV) isopropoxide (Sigma Aldrich 97%), P3HT (Sigma-Aldrich 99.0%), ([6, 6]-phenyl-C61-butyric acid methyl ester, Nano-C purity 99.95%), BCP (2,9-dimethyl-4,7-diphenyl-]1, 10-phenanthroline, 96%, Sigma), indium tin oxide coated glass substrates (25–30 Ω sq^{-1} KINTEC).

NiO_x solution was prepared by admixing 124 mg of nickel (II) acetate tetrahydrate in 5 ml of isopropanol and 30 μl monoethanolamine mixture and this solution was stirred at 70 °C for 4 h [3]. NiO_x precursor was used at room temperature and filtered with a 0.22 μm PTFE filter before coating. TiO_2 precursor was obtained by blending two different solutions in an ice bath. Firstly, 735 μl of titanium (IV) isopropoxide was added into 5 ml of isopropanol. Separately, 70 μl HCl was introduced into 5 ml of isopropanol. Lastly, acidic mixture drop by drop was added into the TTIP: IPA solution at low temperature (5 °C–15 °C) and final precursor was magnetically stirred for 30 min. The resulting transparent TiO_2 precursor was filtered by a 0.45 μm PVDF filter before the deposition. Perovskite solution was obtained by dissolving 1.35 M of PbI_2 and 1.35 M MAI in gamma-butyrolactone at 65 °C for at least 6 h. Filtered with a 0.45 μm PVDF filter before coating. P3HT solution was prepared in chlorobenzene with a 10 mg ml^{-1} concentration and PCBM solution was prepared in chlorobenzene: dichlorobenzene mixture with a 20 mg ml^{-1} concentration. BCP solution was obtained by dissolving 0.5 mg BCP in absolute ethanol.

1.5 cm $\times$ 1.5 cm ITO-coated glass substrates were etched and then sequentially cleaned in acetone and IPA using an

ultrasonic bath. Before NiO_x layer coating ITO-coated substrates were dried with N_2 and cold NiO_x precursor was cast at 1500 rpm for 30 s in ambient air. Coated layers left on a hot plate at 80 °C for 90 s and coating repeated keeping solvent and substrate at room temperature. Finally, coated HTLs were annealed at 450 °C for 30 min in an air furnace. The perovskite solution was kept at 75 °C and cast on warm substrates (held at 100 °C on a hot plate, see figure S4), at 2000 rpm for 10 s and 4500 rpm for 20 s. During the second spinning step, 100 μl of washing solvent (toluene or 1-Pentanethiol: toluene mixture) was dropped instantly on the spinning substrate. The resulting perovskite layers were annealed on a hot plate at 100 °C for 20 min for complete crystallization. For solar cell fabrication 20 mg ml^{-1} PCBM electron transport layer solution was cast on perovskite layers as soon as possible at 2000 rpm for 35 s and dried at 90 °C for 90 s. Further BCP layers were deposited at 4000 rpm for 40 s. For hole-only devices, P3HT hole transport layer was cast on perovskite layer instead of PCBM and BCP layers, at 4000 rpm for 30 s and dried at 90 °C for 10 min. For electron-only devices, TiO_2 substrates were employed instead of NiO_x layers. Compact TiO_2 layers were deposited on ITO substrates at 3000 rpm for 30 s, dried on a hot plate at 100 °C for 30 s then annealed in an air furnace at 475 °C for 30 min. The perovskite coating step was repeated under the same conditions and further, a 10 mg ml^{-1} PCBM electron transport layer solution was cast on perovskite layers at 2000 rpm for 30 s and followed by coating BCP buffer layers at 4000 rpm for 40 s. Fabrication of all devices was completed by a 100 nm thick Ag contact deposition in a high vacuum chamber ($<5 \times 10^{-6}$ Torr) with a shadow mask area of 18 mm^2 (figure S3(a)). Except for metal contact evaporation, whole fabrication was carried out in ambient air under 50%–60% RH and 16 °C–20 °C environment temperature.

X-ray diffraction analysis (XRD) was performed using a PANalytical X'Pert PRO diffractometer. X-ray photoelectron spectroscopy (XPS) analysis was carried out by a Specs-Flex model x-ray photoelectron spectrometer. Optical absorbance spectra were recorded by a PG Instruments T80 UV/VIS spectrophotometer with a resolution of 2 nm between 320 and 1100 nm. Steady-state photoluminescence spectra were recorded by utilizing a-Si photodiode under an Argon ion laser excitation at 514 nm using the standard lock-in amplifier technique. Field emission/low vacuum scanning electron microscopy (FE-SEM) was employed using the FEI Versa 3D scanning electron microscope. The spectral photoconductivity measurements were carried out by using a Thorlabs SLS201L/M broadband halogen lamp and the wavelengths were dispersed by an Acton Research SpectroPro-2500i monochromator and the data were recorded with an SR-830 lock-in-amplifier. The current density–voltage curves of the samples (solar cell, and hole-only devices) were recorded in a glove-box operating a Keithley 2400 model measurement unit. 200 mV s^{-1} scan rate with a 0.03 delay time was used for current–voltage recordings for solar cell device characterizations under an ABET solar simulator (100 mW cm^{-2}, AM 1.5G).

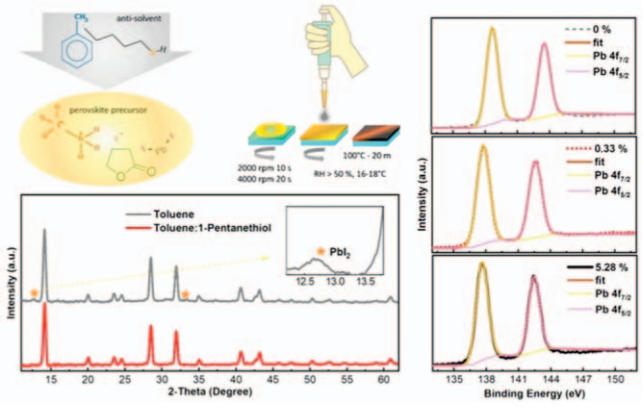


Figure 1. (a) anti-solvent washing route (b) XRD results for perovskite layers on ITO/NiOx substrates using toluene (up) and toluene: 1-Pentanethiol 0.33% (down) anti-solvents (c) XPS curves for perovskite layers using different amounts of 1-Pentanethiol.

Results and discussion

Additive engineering is correlated to hydrogen and covalent bonds between cationic and anionic species in perovskite precursor which might result in intermediate phases and then ends with higher quality formation. Hydrogen bonds are moderately weaker compared to others yet they undertake an important role during perovskite formation. They form between hydrogen and other electronegative atoms (such as nitrogen, oxygen) and affect crystal growth and layer quality. On the other hand, covalent bonds are conveyed as coordinate bonds. As an example, metal cation and water bonding in metal aquo-complexes are defined as coordinate bonds whereas metal–ligand interactions in organometallics [46]. Uncoordinated Pb^{2+} species in $CH_3NH_3PbI_3$ are known to have empty 6p electron orbits. Thus lone electron pair electrons available in another hybridized orbital have the capability of forming coordination bonds where required. This type of lone pair electrons delocalizes into the 6p empty orbit of Pb^{2+} and can form coordination bond [47] in 1-Pentanethiol are presumed to be delocalized by empty Pb^{2+} ions through coordination bonds. Lone pair electrons in 1-Pentanethiol are presumed to be delocalized by empty Pb^{2+} ions through coordination bonds.

The employed anti-solvents and perovskite precursor composition with their molecular structures were given in figure 1(a).

XRD patterns of the reference (toluene) and champion (toluene: 1-Pentanethiol (0.33%)) cells' absorbers were depicted in figure 1(b). XRD results confirmed the formation of the tetragonal structure of $CH_3NH_3PbI_3$ perovskite with diffraction peaks given in table S1 [48]. Weak diffraction peaks were obtained around 12.68° and 33.36° related to the PbI_2 phase in $CH_3NH_3PbI_3$ for the toluene anti-solvent employed layers while these peaks disappeared by 1-Pentanethiol addition into the washing solvent. This might be an indication that 1-Pentanethiol can connect with uncoordinated Pb^{2+} thus resulting in enhanced phase purity of $CH_3NH_3PbI_3$. X-ray photoelectron spectroscopy curves were presented in figure 1(c), for perovskite layers on NiO_x

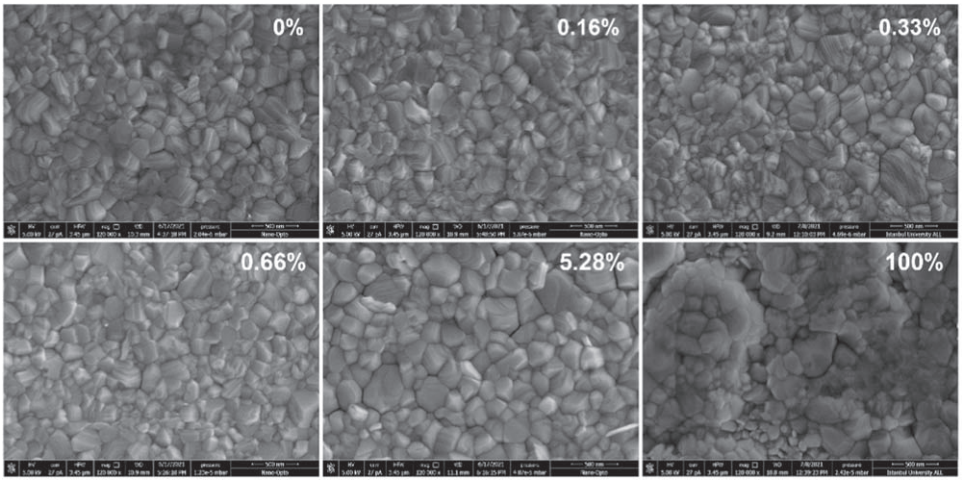


Figure 2. Top-view SEM images of perovskite layers on ITO/NiO_x substrates using different volume ratios of 1-Pentanethiol in toluene (scale is 500 nm).

substrates using 0, 0.33 and, 5.28% 1-Pentanethiol including anti-solvents. Sol–gel-based perovskite growths are commonly polycrystalline and have remarkably high defect densities compared to their single crystalline counterparts. Uncoordinated Pb^{2+} and metallic Pb° are the main destructive types of these defects. Uncoordinated Pb^{2+} species are mostly induced during annealing according to the volatility of organic solvents. Metallic Pb° are assumably chosen to localize to perovskite surface and come with undesired non-radiative recombination processes [49, 50]. Over XPS analysis binding energy differences of uncoordinated Pb^{2+} were scrutinized for surface Pb-4f core levels. While there was no trace for metallic Pb° clusters [27], observed Pb $4f_{7/2}$, and Pb $4f_{5/2}$ peaks exhibited a blue shift in binding energies by the effect of 1-Pentanethiol incorporation. This shift can be explained as a validation of the interaction of 1-Pentanethiol with uncoordinated Pb^{2+} [51, 52]. Moreover, FTIR transmittance spectra are given in figure S1(a). for 0 and 0.33% 1-Pentanethiol employed samples. 1-Pentanethiol incorporated layer exhibited slight shifts (for C=N, C=O) to lower wavenumbers indicating the interaction between 1-pentaniol and Pb^{2+} and passivation of electronic defects [53].

SEM top-view images of $CH_3NH_3PbI_3$ layers on NiO_x substrates with a 120 000 X magnification were shown in figure 2 for various percentages of 1-Pentanethiol in toluene anti-solvent. Up to 5.28% of 1-Pentanethiol content (for reference, 0.16, 0.33, and 0.66%) perovskite morphologies seem to be comparable with the slightly raised number of larger grains concurrently come with the smaller ones. 5.28% of 1-Pentanethiol content resulted in a maximum number of larger grains thus a homogenous distribution of grain widths. For fully 1-Pentanethiol washed samples, large grains were discovered in a vortex form with tiny grains surrounding them.

This might be related to the migration ability of 1-Pentanethiol compared to the toluene due to higher boiling point and slightly lower density of 1-Pentanethiol as compared to that of toluene, which led to degraded perovskite growth quality. Halide perovskites are known to be photoconductive in the literature for a long time. Their efficient photocarrier generation gives rise to positive photoconductivity [54]. As depicted in figure 3(a), all samples show a photoconductivity edge at the 1.65 eV corresponding to the band-gap of tet-p (C−N bonds in MA^+ distribute in a parallel way) phase $CH_3NH_3PbI_3$. The PC spectra show an increasing profile up to 2.2 eV and then fall down due to the high surface recombination at the higher photon energies [55]. While all PC spectra except the 0.33% 1-Pentanethiol employed layers have the same profile in the whole examined range, the 0.33% 1-Pentanethiol shows a second PC edge at 1.82 eV which is reported for the tet-v phase of the $CH_3NH_3PbI_3$. The slightly higher carrier mobilities at the tet-v phase may pave the way to superior power conversion efficiency than the other samples [56]. In addition to the PC measurements, UV–vis absorption spectra of the same samples were obtained to investigate the Urbach energies that can be linked to trap-states, figure S1. All samples exhibited parallel absorption behavior with a band edge of about 770 nm which corresponds to 1.61 eV and also extracted Urbach energies given as an inset.

Similar to the PC results 0.33% 1-Pentanethiol employed perovskite layer exhibited diverging results with the lowest Urbach energy, indicating more inferior band edge disorder and defect density [57, 58]. In other words, Urbach energies started to decrease from 159 meV for pristine layers by increasing 1-Pentanethiol content up to 0.33% (129 meV) and then turned to rise after 0.66%.

Steady-state PL measurements were performed to scan non-radiative recombination within the perovskite layer with/without 1-Pentanethiol. Figure 3(b). showed that emission wavelength around 770 nm with a grander intensity for 1-Pentanethiol incorporated perovskite layers, signifying suppressed non-radiative recombination and thus responsible defects and trap-states [26, 38, 58–61].

Another way to examine defect states and charge dynamics between perovskite and charge transport layers is the space charge limited current (SCLC) method using hole-only or electron-only devices [62]. Figures 3(c) and (d) display the dark current curves of the hole-only and electron-

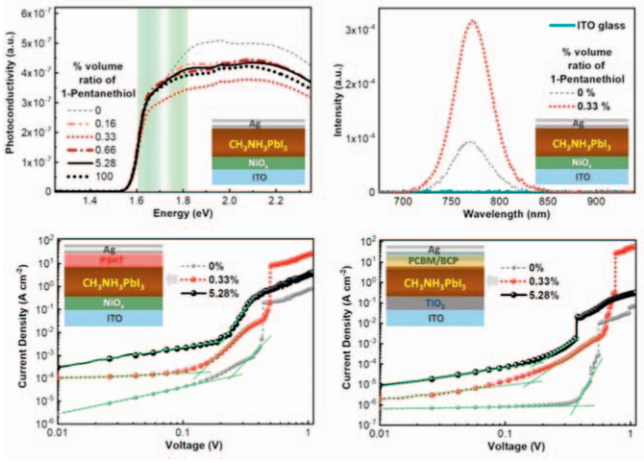


Figure 3. (a) Photoconductivity curves of the perovskite layers (b) dark *J*–*V* curves of the hole only devices (c) dark *J*–*V* curves of the electron only devices.

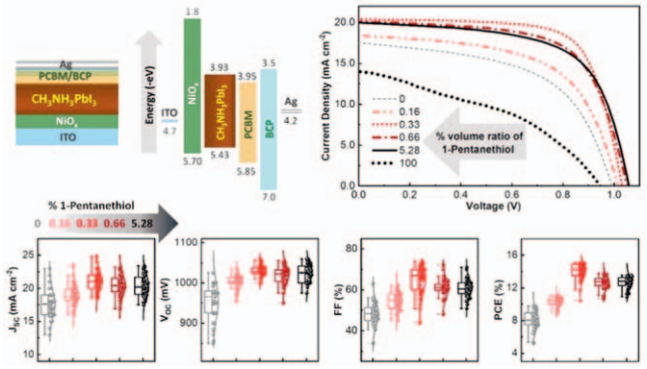


Figure 4. (a) Schematics of device structure (b) illuminated *J*–*V* curves of perovskite solar cells (c) photovoltaic parameters.

only devices where the perovskite layer is sandwiched between NiO_x-P3HT and TiO_2-PCBM, respectively. SCLC curves usually possess three separate parts that begin with the Ohmic region at low bias, continue with a non-linear trap-filled region, and end with the space-charge limited current region. Trap-densities can be calculated by $V_{TFL} = eN_{trap}L^2/2\varepsilon_0\varepsilon_r$ equation using experimentally extracted the V_{TFL} voltages from the intersection of Ohmic and trap-filled regions (as shown by the intersection of the green lines in figures 3(c) and (d)) [53, 63].

Here N_{trap}, L (320 nm, figure S2), ε_o (8.854×10^{-12} F m^{-1}), ε_r (32) [64], and e (1.6×10^{-19} C) terms correspond to trap-density, the thickness of the perovskite layer, vacuum permittivity, the relative dielectric constant of the perovskite, and elementary charge, respectively. V_{TFL} voltages were found to be around 0.244 V, 0.138 V, and 0.200 V for 0, 0.33, and 5.28% 1-Pentanethiol including hole-only devices, respectively. Hence the trap-densities in studied hole-only devices were calculated as 8.44×10^{15} cm^{-3}, 4.77×10^{15} cm^{-3}, and 6.92×10^{15} cm^{-3} for 0, 0.33, and 5.28% 1-Pentanethiol including hole-only devices, respectively. Similarly for electron-only devices, V_{TFL} voltages were seen as 0.365 V, 0.157 V, and 0.179 V for 0, 0.33, and 5.28% 1-Pentanethiol employed devices, respectively. Therefore the trap-densities in electron-only devices were calculated as 12.62×10^{15} cm^{-3}, 5.43×10^{15} cm^{-3}, and 6.19×10^{15} cm^{-3} for 0, 0.33, and 5.28% 1-Pentanethiol including hole-only devices, respectively. The lowest trap-density values were found for both electron and hole-only devices in the case of 0.33% 1-Pentanethiol employed. Trap-densities slightly increased by increasing 1-Pentanethiol up to 5.28% indicating that 0.33% 1-Pentanethiol content can be accepted as optimum value for defect passivation.

To assess the passivating effect of 1-Pentanethiol on the photovoltaic performance, perovskite solar cells are fabricated with an inverted planar cell configuration as depicted in figure 4(a), employing the different amount of 1-Pentanethiol, even 100%. Accordingly, current density–voltage curves were recorded under AM 1.5G irradiation at 100 mW cm^{-2} illumination with a reverse scan (±1.5 V), for champion cells were given figure 4(b). Extracted photovoltaic parameters of champion cells are inserted in table 1, and also complete series are presented in box chart graphic form in figure 4(c). Similar to the PC results 0.33% 1-Pentanethiol employed perovskite layer exhibited diverging results with the lowest Urbach energy, indicating more inferior band edge disorder and defect density [57, 58]. In other words, Urbach energies started to decrease from 159 meV for pristine layers by increasing 1-Pentanethiol content up to 0.33% (129 meV) and then turned to rise after 0.66%.

Steady-state PL measurements were performed to scan non-radiative recombination within the perovskite layer with/without 1-Pentanethiol. Figure 3(b). showed that emission wavelength around 770 nm with a grander intensity for 1-Pentanethiol incorporated perovskite layers, signifying suppressed non-radiative recombination and thus responsible defects and trap-states [26, 38, 58–61]. Moreover, PL measurements repeated for HTL-free layers yielded similar PL intensities with the same behavior, revealing the effect of 1-Pentanethiol. Another way to examine defect states and charge dynamics between perovskite and charge transport layers is the SCLC method using hole-only or electron-only devices [62]. Figures 3(c) and (d) display the dark current curves of the hole-only and electron-only devices where the perovskite layer is sandwiched between NiO_x-P3HT and TiO_2-PCBM, respectively. SCLC curves usually possess three separate parts that begin with the Ohmic region at low bias, continue with a non-linear trap-filled region, and end with the space-charge limited current region. Trap-densities can be calculated by $V_{TFL} = eN_{trap}L^2/2\varepsilon_0\varepsilon_r$ equation using experimentally extracted the V_{TFL} voltages from the intersection of Ohmic and trap-filled regions (as shown by the intersection of the green lines in figures 3(c) and (d)) [53, 63].

Here N_{trap}, L (320 nm, figure S2), ε_o (8.854×10^{-12} F m^{-1}), ε_r (32) [64], and e (1.6×10^{-19} C) terms correspond to trap density, the thickness of the perovskite layer, vacuum permittivity, the relative dielectric constant of the perovskite, and elementary charge, respectively. V_{TFL} voltages were found to be around 0.244 V, 0.138 V, and 0.200 V for 0, 0.33, and 5.28% 1-Pentanethiol including hole-only devices, respectively. Hence the trap densities in studied

Table 1. Photovoltaic parameters of devices with different anti-solvents.

Device[a] Thiol[b]%	V_{OC} (mV)	J_{SC} (mA cm^{-2})	FF (%)	PCE (%)	R_{shunt} (kΩ cm^{-2})	R_{series} (Ω cm^{-2})
0	992 (954)	17.50 (17.58)	56.3 (48.0)	9.77 (8.06)	3.97	16.00
0.16	1014 (1002)	18.36 (18.93)	59.8 (54.5)	11.13 (10.29)	6.41	15.28
0.33	1032 (1029)	20.40 (21.13)	71.5 (65.1)	15.05 (14.08)	20.90	6.85
0.66	1052 (1019)	20.11 (20.41)	65.0 (61.1)	13.75 (12.64)	7.75	10.79
5.28	1060 (1025)	19.95 (20.36)	63.9 (60.8)	13.51 (12.69)	6.02	8.71
100	944	14.00	41.1	5.43	1.28	37.31

[a] ITO/NiO_x (22 nm) /$CH_3NH_3PbI_3$ (320 nm) /PCBM/BCP (100 nm)/Ag (110 nm).
[b] 1-PentanethiolAverage values over 32 cells are given in parenthesis.

hole-only devices were calculated as 8.44×10^{15} cm^{-3}, 4.77×10^{15} cm^{-3}, and 6.92×10^{15} cm^{-3} for 0, 0.33, and 5.28% 1-Pentanethiol including hole-only devices, respectively. Similarly for electron-only devices, V_{TFL} voltages were seen as 0.365 V, 0.157 V, and 0.179 V for 0, 0.33, and 5.28% 1-Pentanethiol employed devices, respectively. Therefore the trap densities in electron-only devices were calculated as 12.62×10^{15} cm^{-3}, 5.43×10^{15} cm^{-3}, and 6.19×10^{15} cm^{-3} for 0, 0.33, and 5.28% 1-Pentanethiol including hole-only devices, respectively. The lowest trap density values were found for both electron and hole-only devices in the case of 0.33% 1-Pentanethiol employed. Trap densities slightly increased by increasing 1-Pentanethiol up to 5.28% indicating that 0.33% 1-Pentanethiol content can be accepted as optimum value for defect passivation.

To assess the passivating effect of 1-Pentanethiol on the photovoltaic performance, perovskite solar cells are fabricated with an inverted planar cell configuration as depicted in figure 4(a), employing the different amount of 1-Pentanethiol, even 100%. Accordingly, current density–voltage curves were recorded under AM 1.5G irradiation at 100 mW cm^{-2} illumination with a reverse scan (±1.5 V), for champion cells were given figure 4(b). Extracted photovoltaic parameters of champion cells are inserted in table 1, and also complete series are presented in box chart graphic form in figure 4(c).

An increasing trend was heeded in the open-circuit voltage values by 1-Pentanethiol incorporation that reveals a top for 0.33% content over average V_{OC}s (given in parenthesis), which is known to be enriched by the decreased amount of unreacted PbI_2. Fill factor values were obviously improved by 1-Pentanethiol incorporation and showed a slight decrease after 0.66%, with a similar manner of short circuit current densities. As a result, 0.33% volume ratio was encountered to be optimum for 1-Pentanethiol enhancement on the perovskite growth process, resulting in a 35.6% FF, 20.2% J_{SC}, and 74.7% PCE increment over average values. Furthermore, series and shunt resistance values (table 1) indicated a more suitable coverage with a homogenous structure in addition to the lessened trap-densities for 0.33% 1-Pentanethiol content, linked to the highest R_{shunt} and lowest R_{series} value.

Histogram of the cell efficiencies with a Gaussian distribution are portrayed in figure S3(b), for various 1-Pentanethiol contents while the aging of the reference and optimum 1-Pentanethiol including devices is shown in figure S4(b). Both reference and 1-Pentanethiol modified cells kept their PCEs up to 60% for over 2 weeks under dark and moderate humidity conditions (RH > 50%). However, reference cells lost 40% of initial efficiencies after 30 weeks while 1-Pentanethiol containing cells still kept their initial PCEs over 60%. These results denote that 1-Pentanethiol enhancement of the photovoltaic performances came with increased stability over 5000 h without encapsulation.

Conclusion

Single-cation perovskites, represented by their more straightforward composition involving fewer elements and streamlined synthesis methodologies, hold reduced production costs, making them especially appealing for large-scale applications. The precise synthesis process of single-cation perovskites aligns with the demand for cost-effective production methods, contributing to their attractiveness for industrial scalability. While triple-cation perovskites provide band gap tuning, our study focus on single-cation perovskites arises from their unique ability to fulfill specific application requirements. The engineered properties of single-cation perovskites, in conjunction with their economic feasibility, make them advantageous.

Here we report a successful ambient air fabrication of fully solution prepared inverted $CH_3NH_3PbI_3$ perovskite solar cells by 1-Pentanethiol modification. By this modification, a PCE increment of 54% was observed with refinement in long-term stability under ambient conditions without encapsulation. Even though thiol-related molecules are employed as interface passivation layers for perovskite solar cells, there is no work related to 1-Pentanethiol. Moreover, involvement of thiol during washing is presented for the first time by resulting in a hindered level of the unreacted PbI_2 and also reduced trap-densities. We believe that our results are promising in the field for the potential use of the 1-Pentanethiol for perovskite solar fabrication, which could induce record PCEs under glove-box conditions.

Acknowledgments

This work is supported by Istanbul University Scientific Research Projects Coordination under the Grant No. FAB-2021-37975.

Data availability statement

The data cannot be made publicly available upon publication because no suitable repository exists for hosting data in this field of study. The data that support the findings of this study are available upon reasonable request from the authors.

Supplementary material

Additional information on material synthesis, structural characterization, and cell durability is provided in the supplementary material, detailing the methods and results obtained.

ORCID iDs

F Pinar Gokdemir Choi https://orcid.org/0000-0003-3048-6534
Furkan Kuruoğlu https://orcid.org/0000-0002-5314-4441
Ayse Erol https://orcid.org/0000-0003-4196-1791

References

[1] Yoo J J *et al* 2021 Efficient perovskite solar cells via improved carrier management *Nature* **590** 587–93
[2] Jeng J Y, Chiang Y F, Lee M H, Peng S R, Guo T F, Chen P and Wen T C 2013 $CH_3NH_3PbI_3$ perovskite/fullerene planar-heterojunction hybrid solar cells *Adv. Mater.* **25** 3727–32
[3] Adhikari N, Dubey A, Gaml E A, Vaagensmith B, Reza K M, Mabrouk S A A, Gu S, Zai J, Qian X and Qiao Q 2016 Crystallization of a perovskite film for higher performance solar cells by controlling water concentration in methyl ammonium iodide precursor solution *Nanoscale* **8** 2693–703
[4] Choi W G, Kang D W, Na S, Park C G, Gokdemir F P and Moon T 2018 Sequentially vapor-grown hybrid perovskite for planar heterojunction solar cells *Nanoscale Res. Lett.* **13** 1–6
[5] Choi W G, Park C G, Kim Y and Moon T 2020 Sn perovskite solar cells via 2D/3D bilayer formation through a sequential vapor process *ACS Energy Lett.* **5** 3461–7
[6] Im J H, Kim H S and Park N G 2014 Morphology-photovoltaic property correlation in perovskite solar cells: one-step versus two-step deposition of $CH_3NH_3PbI_3$ *Apl. Mater.* **2** 081510
[7] Ahmadian-Yazdi M R, Zabihi F, Habibi M and Eslamian M 2016 Effects of process parameters on the characteristics of mixed-halide perovskite solar cells fabricated by one-step and two-step sequential coating *Nanoscale Res. Lett.* **11** 408
[8] Carnie M J, Charbonneau C, Davies M L, Troughton J, Watson T M, Wojciechowski K, Snaith H and Worsley D A 2013 A one-step low temperature processing route for organolead halide perovskite solar cells *Chem. Commun.* **49** 7893–5
[9] Lewis A E, Zhang Y, Gao P and Nazeeruddin M K 2017 Unveiling the concentration-dependent grain growth of perovskite films from one and two-step deposition methods: implications for photovoltaic application *ACS Appl. Mater. Interfaces* **9** 25063–6
[10] Eperon G E, Burlakov V M, Docampo P, Goriely A and Snaith H J 2014 Morphological control for high performance, solution-processed planar heterojunction perovskite solar cells *Adv. Funct. Mater.* **24** 151–7
[11] Jeon N J, Noh J H, Kim Y C, Yang W S, Ryu S and Seok S I 2014 Solvent engineering for high-performance inorganic-organic hybrid perovskite solar cells *Nat. Mater.* **13** 897–903
[12] Jeon N J, Noh J H, Yang W S, Kim Y C, Ryu S, Seo J and Seok S I 2015 Compositional engineering of perovskite materials for high-performance solar cells *Nature* **517** 476–80
[13] Taylor A D, Sun Q, Goetz K P, An Q, Schramm T, Hofstetter Y, Litterst M, Paulus F and Vaynzof Y 2021 A general approach to high-efficiency perovskite solar cells by any antisolvent *Nat. Commun.* **12** 1878
[14] Ghosh S, Mishra S and Singh T 2020 Antisolvents in perovskite solar cells: importance, issues, and alternatives *Adv. Mater. Interfaces* **7** 2000950
[15] Zhang H, Niu Q, Tang X, Wang H, Huang W, Xia R, Zeng W, Yao J and Yan B 2017 Understanding the effect of delay time of solvent washing on the performances of perovskite solar cells *ACS Omega* **2** 7666–71
[16] Taherianfard H, Kim G W, Byranvand M M, Choi K, Kang G, Choi H, Tajabadi F, Taghavinia N and Park T 2020 Effective management of nucleation and crystallization processes in perovskite formation via facile control of antisolvent temperature *ACS Appl. Energy Mater.* **3** 1506–14
[17] Park M, Kim J Y, Son H J, Lee C H, Jang S S and Ko M J 2016 Low-temperature solution-processed Li-doped SnO_2 as an effective electron transporting layer for high-performance flexible and wearable perovskite solar cells *Nano Energy* **26** 208–15
[18] Chen S, Xiao X, Chen B, Kelly L L, Zhao J, Lin Y, Toney M F and Huang J 2021 Crystallization in one-step solution deposition of perovskite films: upward or downward? *Sci. Adv.* **7** eabb2412
[19] Huang P H, Wang Y H, Ke J C and Huang C J 2017 The effect of solvents on the performance of $CH_3NH_3PbI_3$ perovskite solar cells *Energies* **10** 599
[20] Long J, Sheng W, Dai R, Huang Z, Yang J, Zhang J, Li X, Tan L and Chen Y 2020 Understanding the mechanism between antisolvent dripping and additive doping strategies on the passivation effects in perovskite solar cells *ACS Appl. Mater. Interfaces* **12** 56151–60
[21] Mahapatra A, Prochowicz D, Tavakoli M M, Trivedi S, Kumar P and Yadav P 2020 A review of aspects of additive engineering in perovskite solar cells *J. Mater. Chem.* A **8** 27–54
[22] Lee J W, Kim H S and Park N G 2016 Lewis acid-base adduct approach for high efficiency perovskite solar cells *Acc. Chem. Res.* **49** 311–9
[23] Deng X, Xie L, Wang S, Li C, Wang A, Yuan Y, Cao Z, Li T, Ding L and Hao F 2020 Ionic liquids engineering for high-efficiency and stable perovskite solar cells *Chem. Eng. J.* **398** 125594
[24] Li N *et al* 2019 Cation and anion immobilization through chemical bonding enhancement with fluorides for stable halide perovskite solar cells *Nat. Energy* **4** 408–15
[25] Noel N K, Abate A, Stranks S D, Parrott E S, Burlakov V M, Goriely A and Snaith H J 2014 Enhanced photoluminescence and solar cell performance via Lewis base passivation of organic-inorganic lead halide perovskites *ACS Nano* **8** 9815–21
[26] Wang J, Zhang J, Zhou Y, Liu H, Xue Q, Li X, Chueh cc, Yip H L, Zhu Z and Jen A K Y 2020 Highly efficient all-inorganic perovskite solar cells with suppressed non-radiative recombination by a Lewis base *Nat. Commun.* **11** 177

[27] Wu T, Wang Y, Li X, Wu Y, Meng X, Cui D, Yang X and Han L 2019 Efficient defect passivation for perovskite solar cells by controlling the electron density distribution of donor-π-acceptor molecules *Adv. Energy Mater.* **9** 1803766

[28] Hamill J C, Romiluyi O, Thomas S A, Cetola J, Schwartz J, Toney M F, Clancy P and Loo Y L 2020 Sulfur-donor solvents strongly coordinate Pb^{2+} in hybrid organic-inorganic perovskite precursor solutions *J. Phys. Chem.* C **124** 14496–502

[29] Wharf I, Gramstad T, Makhija R and Onyszchuk M 1976 Synthesis and vibrational spectra of some lead(II) halide adducts with O, S, and N-donor atom ligands *Can. J. Chem.* **54** 3430–8

[30] Min H, Kim G, Paik M J, Lee S, Yang W S, Jung M and Seok S I 2019 Perovskite solar cells: stabilization of precursor solution and perovskite layer by addition of sulfur (Adv. Energy Mater. 17/2019) *Adv. Energy Mater.* **9** 1970056

[31] Leblanc A, Mercier N, Allain M, Dittmer J, Pauporté T, Fernandez V, Boucher F, Kepenekian M and Katan C 2019 Enhanced stability and band gap tuning of α-$[HC(NH_2)_2]PbI_3$ hybrid perovskite by large cation integration *ACS Appl. Mater. Interfaces* **11** 20743–51

[32] Zhou Y, Liu C, Meng F, Zhang C, Wei G, Gao L and Ma T 2021 Recent progress in perovskite solar cells modified by sulfur compounds *Sol. RRL* **5** 2000713

[33] Zhou T, Lai H, Liu T, Lu D, Wan X, Zhang X, Liu Y and Chen Y 2019 Highly efficient and stable solar cells based on crystalline oriented 2D/3D hybrid perovskite *Adv. Mater.* **31** 1901242

[34] Cao J, Yin J, Yuan S, Zhao Y, Li J and Zheng N 2015 Thiols as interfacial modifiers to enhance the performance and stability of perovskite solar cells *Nanoscale* **7** 9443–7

[35] Chang C Y, Chang Y C, Huang W K, Lee K T, Cho A C and Hsu cc 2015 Enhanced performance and stability of semitransparent perovskite solar cells using solution-processed thiol-functionalized cationic surfactant as cathode buffer layer *Chem. Mater.* **27** 7119–27

[36] Chang C Y, Chang Y C, Huang W K, Liao W C, Wang H, Yeh C, Tsai B C, Huang Y C and Tsao C S 2016 Achieving high efficiency and improved stability in large-area ITO-free perovskite solar cells with thiol-functionalized self-assembled monolayers *J. Mater. Chem.* A **4** 7903–13

[37] Li Z, Zhu Z, Chueh cc, Luo J and Jen A K Y 2016 Facile thiol-ene thermal crosslinking reaction facilitated hole-transporting layer for highly efficient and stable perovskite solar cells *Adv. Energy Mater.* **6** 1601165

[38] Xu H, Liu G, Xu X, Xu S, Zhang L, Chen X, Zheng H and Pan X 2020 Hydrophobic 2D perovskite-modified layer with polyfunctional groups for enhanced performance and high moisture stability of perovskite solar cells *Sol. RRL* **4** 2000647

[39] Wu S *et al* 2020 2D metal–organic framework for stable perovskite solar cells with minimized lead leakage *Nat. Nanotechnol.* **15** 934–40

[40] Ruan L, Shen W, Wang A, Xiang A and Deng Z 2017 Alkyl-Thiol ligand-induced shape and crystalline phase-controlled synthesis of stable perovskite-related $CsPb_2Br_5$ nanocrystals at room temperature *J. Phys. Chem. Lett.* **8** 3853–60

[41] Shi Y, Zhang H, Tong X, Hou X, Li F, Du Y, Wang S, Zhang Q, Liu P and Zhao X 2021 Interfacial engineering via self-assembled thiol silane for high efficiency and stability perovskite solar cells *Sol. RRL* **5** 2100128

[42] Xiao G-B, Wang L-Y, Mu X-J, Zou X-X, Wu Y-Y and Cao J 2021 Lead and iodide fixation by thiol copper(II) porphyrin for stable and environmental-friendly perovskite solar cells *CCS Chem.* **3** 25–36

[43] Li C, Wang L, Yan P J, Liu H, Cao J, Chen cc and Tang Y 2021 Perovskite surface management by thiol and amine copper porphyrin for stable and clean solar cells *Chem. Eng. J.* **409** 128167

[44] Fateev S A, Petrov A A, Khrustalev V N, Dorovatovskii P V, Zubavichus Y V, Goodilin E A and Tarasov A B 2018 Solution processing lof methylammonium lead iodide perovskite from γ-butyrolactone: crystallization mediated by solvation equilibrium *Chem. Mater.* **30** 5237–44

[45] Seo Y H, Kim E C, Cho S P, Kim S S and Na S I 2017 High-performance planar perovskite solar cells: Influence of solvent upon performance *Appl. Mater. Today* **9** 598–604 (https://nature.com/articles/s41586-021-03285-w)

[46] Yang J, Chen S, Xu J, Zhang Q, Liu H, Liu Z and Yuan M 2019 A review on improving the quality of perovskite films in perovskite solar cells via the weak forces induced by additives *Appl. Sci. (Switzerland)* **9** 4393

[47] Laskar M A R *et al* 2020 Phenylhydrazinium iodide for surface passivation and defects suppression in perovskite solar cells *Adv. Funct. Mater.* **30** 2000778

[48] Oku T 2015 Crystal structures of $CH_3NH_3PbI_3$ and related perovskite compounds used for solar cells *Solar Cells—New Approaches Rev.* **1** 77–103

[49] Kerner R A, Schloemer T H, Schulz P, Berry J J, Schwartz J, Sellinger A and Rand B P 2019 Amine additive reactions induced by the soft Lewis acidity of Pb^{2+} in halide perovskites: II. Impacts of amido Pb impurities in methylammonium lead triiodide thin films *J. Mater. Chem.* C **7** 5244–50

[50] Kirakosyan A, Chinh N D, Sihn M R, Jeon M G, Jeong J R, Kim D, Jang J H and Choi J 2019 Mechanistic insight into surface defect control in perovskite nanocrystals: ligands terminate the valence transition from Pb^{2+} to metallic Pb^0 *J. Phys. Chem. Lett.* **10** 4222–8

[51] Wu Z, Jiang M, Liu Z, Jamshaid A, Ono L K and Qi Y 2020 Highly efficient perovskite solar cells enabled by multiple ligand passivation *Adv. Energy Mater.* **10** 1903696

[52] Li M, Yu L, Zhang Y, Gao H, Li P, Chen R and Huang W 2020 Multiple passivation of electronic defects for efficient and stable perovskite solar cells *Sol. RRL* **4** 2000481

[53] Guo Y, Ma J, Lei H, Yao F, Li B, Xiong L and Fang G 2018 Enhanced performance of perovskite solar cells: via anti-solvent nonfullerene Lewis base IT-4F induced trap-passivation *J. Mater. Chem.* A **6** 5919–25

[54] Haque M A, Li J L, Abdelhady A L, Saidaminov M I, Baran D, Bakr O M, Wei S H and Wu T 2019 Transition from positive to negative photoconductance in doped hybrid perovskite semiconductors *Adv. Opt. Mater.* **7** 1900865

[55] Khenkin M V, Amasev D V, Kozyukhin S A, Sadovnikov A V, Katz E A and Kazanskii A G 2017 Temperature and spectral dependence of $CH_3NH_3PbI_3$ films photoconductivity *Appl. Phys. Lett.* **110** 222107

[56] Geng W, Zhang L, Zhang Y N, Lau W M and Liu L M 2014 First-principles study of lead iodide perovskite tetragonal and orthorhombic phases for photovoltaics *J. Phys. Chem.* C **118** 19565–71

[57] Wu S, Li Z, Zhang J, Liu T, Zhu Z and Jen A K Y 2019 Efficient large guanidinium mixed perovskite solar cells with enhanced photovoltage and low energy losses *Chem. Commun.* **55** 4315–8

[58] Li Z, Wu S, Zhang J, Yuan Y, Wang Z and Zhu Z 2020 Improving photovoltaic performance using perovskite/surface-modified graphitic carbon nitride heterojunction *Sol. RRL* **4** 1900413

[59] Chaudhary B, Kulkarni A, Jena A K, Ikegami M, Udagawa Y, Kunugita H, Ema K and Miyasaka T 2017 Poly(4-Vinylpyridine)-based interfacial passivation to enhance voltage and moisture stability of lead halide perovskite solar cells *Chem. Sus. Chem.* **10** 2473–9

[60] Han Q, Yang S, Wang L, Yu F, Zhang C, Wu M and Ma T 2021 The sulfur-rich small molecule boosts the efficiency of

carbon-based $CsPbI_2Br$ perovskite solar cells to approaching 14% *Sol. Energy* **216** 351–7

[61] Peng Q, Zheng X, Zhang X, You S, Li L, Zhao Y, Zhang S, Luo L, Zeng H and Li X 2020 Radical molecular modulator for high-performance perovskite solar cells *Front. Chem.* **8** 825

[62] Sajedi Alvar M, Blom P W M and Wetzelaer G J A H 2020 Space-charge-limited electron and hole currents in hybrid organic-inorganic perovskites *Nat. Commun.* **11** 4023

[63] Dong Q, Fang Y, Shao Y, Mulligan P, Qiu J, Cao L and Huang J 2015 Electron-hole diffusion lengths >175 μm in solution-grown $CH_3NH_3PbI_3$ single crystals *Science* **347** 967–70

[64] Zhu W, Kang L, Yu T, Lv B, Wang Y, Chen X, Wang X, Zhou Y and Zou Z 2017 Facile face-down annealing triggered remarkable texture development in $CH_3NH_3PbI_3$ films for high-performance perovskite solar cells *ACS Appl. Mater. Interfaces* **9** 6104–13